UNIVERSITY OF TARTU

Faculty of Science and Technology

Institute of Physics

Gulnara Yusibova

Surface Morphology Effects on Bifunctional Oxygen Electroactivity of TAL2-based Materials

Master thesis in Materials Science and Technology

Supervisors:

Assoc. Prof., Nadezda Kongi

Assoc. Prof., Kaido Tammeveski

Tartu 2021

Surface Morphology Effects on Bifunctional Oxygen Electroactivity of TAL2-based Materials

Abstract:

The design and synthesis of active and cost-effective bifunctional electrocatalysts toward oxygen reduction reaction (ORR) and oxygen evolution reaction (OER) are urgent for the applications of metal-air batteries and fuel cells. Nowadays, noble metals and their compounds such as Pt, RuO_2 are appraised as state-of-the-art active materials for oxygen electrocatalysis. However, their extensive use is hindered by scarce resources and high costs. Therefore, developing a novel strategy for facile design and fabrication of low-cost and high-efficient bifunctional non-precious metal-based catalysts is crucial. Inspired by the fast progress of implementing metal-organic framework (MOF)-based materials in different applications, a novel TAL-2-based catalyst material is developed through organic synthesis, pyrolysis, and acid treatment processes. Remarkably, TAL-2-700L1B2 demonstrates excellent electrocatalytic performances with a half-wave potential of 0.844 V for ORR and a potential of 1.58 V at 10 mA cm^{-2} for OER compared to other catalysts of various temperature and treatment which were studied in this work. To investigate active sites and surface morphology of catalyst materials, SEM, PXRD, XPS, and BET analyses were employed. Experimental data collected in this work will further be used for theoretical calculations to understand the structure-electroactivity relationship.

Keywords: Oxygen Reduction Reaction; Oxygen Evolution Reaction; Surface Morphology; Bifunctional Oxygen Electroactivity

CERCS: P401 Electrochemistry

Pinna morfoloogia mõju TAL2-põhiste materjalide bifunktsionaalsele hapniku elektroaktiivsusele

Lühikokkuvõte:

Aktiivsete ja kulutõhusate bifunktsionaalsete elektrokatalüsaatorite disain ja süntees hapniku redutseerimisreaktsiooni (ORR) ja hapniku eraldumisreaktsiooni (OER) jaoks on metall-õhk patareide ja kütuseelementide rakendamiseks hädavajalik. Tänapäeval peetakse väärismetalle ja nende ühendeid nt Pt, RuO_2 kõige aktiivsemateks hapniku elektrokatalüüsi materjalideks, kuid nende laialdast kasutamist takistavad vähesed ressursid ja kõrge hind. Seetõttu on oluline välja töötada strateegia odavamate ja tõhusate bifunktsionaalsete mitteväärismetallidel põhinevate katalüsaatorite valmistamiseks. Inspireerituna metall-orgaanilistel võrestikel (MOF) põhinevate materjalide kiire rakendamise edusammudest, sünteesiti selles töös uudne TAL-2-põhine katalüsaatormaterjal. Erilist tähelepanu pöörati materjali sünteesijärgsele töötlemisele (karboniseerimine ja töötlemine hapetes). Parimaid elektrokatalüütilisi omadusi näitas TAL-2-700L1B2 materjal, mille ORR poollainepotentsiaal oli 0,844 V ja OER potentsiaal 10 mA cm^{-2} juures oli 1,58 V. Katalüsaatormaterjalide aktiivtsentrite ja pinna morfoloogia uurimiseks kasutati SEM, PXRD, XPS ja BET analüüse. Selles töös kogutud eksperimentaalseid andmeid kasutatakse edaspidi teoreetilistes arvutustes, et leida seos materjalide pinnastruktuuri ja hapniku elektroaktiivsuse vahel.

Võtmesõnad: Hapniku redutseerumisreaktsioon; Hapniku eraldumisreaktsioon; Pinna morfoloogia; Bifunktsionaalne hapniku elektroaktiivsus

CERCS: P401 Elektrokeemia

TABLE OF CONTENTS

ABBREVIATIONS

AEM – anion exchange membrane

BET – Brunauer–Emmett–Teller

CNTs – carbon nanotubes

CV – cyclic voltammetry

EIS – electrochemical impedance spectroscopy

GC – glassy carbon

HER – hydrogen evolution reaction

K-L – Koutecký–Levich

M-N-C – transition metal-nitrogen-carbon

MOF – metal-organic framework

OER – oxygen evolution reaction

ORR – oxygen reduction reaction

OVs – oxygen vacancies

PGMs – platinum group metals

PXRD – powder X-ray diffraction

RDE – rotating disk electrode

RHE – reversible hydrogen electrode

SEM – scanning electron microscopy

TM – transition metal

WE – working electrode

XPS – X-ray photoelectron spectroscopy

1. INTRODUCTION

Oxygen reduction reaction (ORR) and oxygen evolution reaction (OER) are known as major reactions for electrochemical energy conversion and storage systems. Currently, precious metals and their compounds such as Pt, RuO_2 are considered as state- of-the-art active materials for oxygen electrocatalysis. However, their high price and insufficient availability limit their extensive use and non-precious metal catalyst materials have been chosen as their potential substitutes for electrocatalysis. The design of very efficient, stable and low-priced bifunctional ORR/OER catalysts plays crucial role in utilizing of this technology at macroscale level.

Due to their rich porous structure and high electrical conductivity, carbon materials containing transitional metal and nitrogen in their structure (M-N-C) are favorable to design very efficient oxygen electrocatalysts. Moreover, the particular class of materials, which are called metal-organic frameworks (MOFs), have appeared as promising precursors to build M-N-C electrocatalysts. In common practice, M-N-C materials undergo post-synthetic treatment, which results in changes in porosity and morphology, distribution of active sites, and acceleration of mass transport in electrocatalytic reactions. In this work novel cobalt-based MOF was synthesized from 1H-benzo[d]imidazole-5,6-diol linker and cobalt precursor and subsequent post-synthetic treatment was optimized to prepare highly active Co-N-C electrocatalyst.

To assist the development of active bifunctional oxygen electrocatalysts, it is necessary to establish simple criteria and relationships between the electroactivity and the surface morphology of electrode material. Therefore, this study focuses on collection of experimental descriptors, which can further be used in prediction of electrochemical activity parameters.

In this thesis 36 different treatment conditions were applied to TAL2-based Co-N-C material and a systematic study of changes in morphology was performed by SEM, Raman, BET, XPS and XRD. All 36 samples were electrochemically tested toward ORR and OER in 0.1 M KOH solution and obtained kinetic parameters were correlated to understand structure vs activity relationship.

2. LITERATURE OVERVIEW

2.1. Oxygen Reduction Reaction (ORR)

Oxygen is the most abundant and one of the essential elements in the Earth`s crust. The oxygen reduction reaction (ORR) is also known as a predominant chemical reaction and has been a concern of large-scale investigation over the past century. This is substantial because the ORR has a leading role in vital processes, specifically biological respiration and in energy-converting systems, notably in a branch of metal-air batteries and fuel cells.

According to the overall electrocatalytic ORR process, two pathways are scrutinized mostly; each process has some distinct steps. One is direct 4-electron reduction pathway from O_2 to H_2O, which can be catalyzed by some chalcogenides, noble metals, noble metal alloy materials, di-nuclear cobalt macrocyclic complexes, transition-metal carbide-promoted Pt catalysts, iron-macrocyclic complexes, etc. The other is partial reduction, implies 2-electron transfer pathway from O_2 to hydrogen peroxide (H_2O_2) and can be promoted by quinones and derivatives, some chalcogenides, mono-nuclear cobalt macrocyclic compounds, carbon nanomaterials, etc. The 1-electron transfer to O_2 produces superoxide anion (O_2^-), which could be observed in a room-temperature ionic liquid system, on specific transition-metals, macrocyclic-compounds-coated graphite electrodes in alkaline solutions and in non-aqueous aprotic systems.[1]

Proposed ORR reaction pathways in alkaline solutions:[2]

$O_2 + 2H_2O + 4e^- \rightleftharpoons 4OH^-$ $\quad E^0 = 0.401$ V vs. SHE

$O_2 + H_2O + 2e^- \rightleftharpoons HO_2^- + OH^-$ $\quad E^0 = -0.076$ V vs. SHE

$HO_2^- + H_2O + 2e^- \rightleftharpoons 3OH^-$ $\quad E^0 = 0.878$ V vs. SHE

or disproportionation of HO_2^-:

$2HO_2^- \rightleftharpoons 2OH^- + O_2$

Proposed ORR reaction pathways in acidic solutions:[2]

$O_2 + 4H^+ + 4e^- \rightleftharpoons 2H_2O$ $\quad E^0 = 1.229$ V vs. SHE

$O_2 + 2H^+ + 2e^- \rightleftharpoons H_2O_2$ $\quad E^0 = 0.695$ V vs. SHE

$H_2O_2 + 2H^+ + 2e^- \rightleftharpoons 2H_2O$ $\quad E^0 = 1.776$ V vs. SHE

$2H_2O_2 \rightleftharpoons 2H_2O + O_2$

Proposed ORR reaction pathways in non-aqueous aprotic solvents:[1]

$O_2 + e^- \rightleftharpoons O_2^-$

$O_2^- + e^- \rightleftharpoons O_2^{2-}$

All these electrochemical reactions have their unique importance, based on applications. The four-electron direct pathway is particularly favorable in both metal-air batteries and fuel cells. In industrial production of H_2O_2, the two-electron transfer process is employed. The one-electron pathway is in the interest of fundamental examination of the ORR mechanism.[1]

Typically, ORR has sluggish kinetics and is affected by pH value of the solution. For instance, ORR shows higher activity in alkaline solution than in acidic media.[3] In order to accelerate the kinetics of the ORR, a cathode catalyst is required. From this perspective, platinum (Pt)-based materials are considered as state-of-the-art catalysts. However, the main bottleneck associated with Pt-based catalysts is their exorbitant costs.[1] As reported by researchers, the catalytic activity of Pt towards the ORR depends on various factors such as the dissociation energy of the O-O bond, the binding energy of OH on the Pt surface and its O_2 adsorption energy, which is affected by either the electronic structure of the Pt catalyst (Pt d-band vacancy), or the Pt-Pt interatomic distance (geometric effect). According to several theoretical calculations corresponding with experimental results, Pt has highest ORR electrocatalytic activity than other noble metals, namely in the order of Pt> Pd> Ir> Rh.[4] Nonetheless, to explore ORR mechanism can assist to comprehend it at molecular level. As stated in Hund`s rule, O_2 holds 2 unpaired electrons in its ground state, which located in a doubly degenerate π^* antibonding orbital that stands for a triplet state and in this case, bond order of oxygen is two. The bonding orbitals of oxygen molecule credit to the 3 σ_g orbital with two electrons. However, doubly degenerate 1 π_g^* and 1 π_u orbitals have single and double occupancy, respectively. As the reduction of O_2 happens, the bond order of O-O becomes lessen due to the filling of antibonding orbitals by the electrons which result in increasing O-O bond distance, and a decrease in vibrational frequency. Evidently, number of excess of bonding over nonbonding electrons is four in the diagram of Figure 1.[4] It elucidates the comparatively low reactivity of the O_2 molecule and its great stability, regardless of its high oxidizing power.[4]

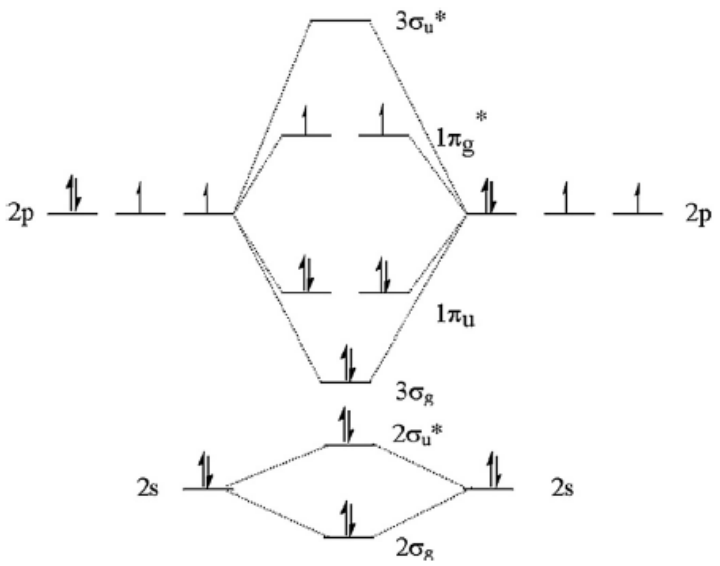

Figure 1. Molecular orbital diagram of oxygen molecule.[4]

Besides, there are some following prerequisites for a good ORR electrocatalysts such as interaction between the catalyst particle and support surface, electrical conductivity, chemical and electrochemical stability (should not be oxidized by oxygen or its reduction intermediates or protons or at high electrode potentials), catalytic activity towards ORR and catalytic stability should be great, while not dissolve in the electrolyte, which means to be insoluble in methanolic solutions, in basic aqueous or acidic solutions. Moreover, it is desirable for chosen catalyst to have propitious morphology, propitious optimum structural composition, uniform spread of catalyst particles on support, tiny particles, high porosity as well as high specific surface area.[5] According to recent studies, some Pt alloys can show enhanced electrocatalytic activity in basic medium such as PtAu/CNT (carbon nanotubes) compared to Pt/CNT. However, Pd-Pt alloy exhibit greatest electrocatalytic activity towards the ORR versus other alloys of Pt due to the fully occupied d-orbital of Pd. In other words, Gibbs free energy eliminated by d-orbital coupling effect amid metals and give rise to improved ORR kinetics. Besides, PdCu, PdCo, PdFe, PdAg are also performed better electrocatalytic activity than Pd alone.[6]

It has been reported that heat-treatment has immense effect to ameliorate activity of catalyst. Heat-treatment can be conducted under inert (Ar, N_2, He) atmospheric condition by heating the catalyst in the temperature range of 80–900 °C during 1-4 h which aims even and stable spreading of catalyst on the support, elimination of impurities from material, hence increasing electrocatalytic activity of the catalyst. Nevertheless, heat-treatment can also improve electrocatalytic activity of alloying of the catalyst by reducing the Pt-Pt distance and thus d-

band vacancy.[6] The oxygen reduction reaction is also examined in alkaline solution employing anion exchange membranes (AEMs) and superb improvement in ORR activity was observed. It is known that plenty of catalysts are available for ORR in alkaline media versus acidic solutions because of corrosive conditions in acidic media. Furthermore, alloys of palladium are relatively better than Pt/C. For example, PdSn applying anion exchange membrane performed brilliant activity in contrast to commercial Pt/C evaluated in proton exchange membrane.[6]

2.2. Oxygen Evolution Reaction (OER)

The oxygen evolution reaction (OER) plays a crucial role in several processes such as water electrolysis to generate oxygen and hydrogen, electrocatalytic evolution of oxygen deriving out of oxoacids and oxides and to produce molecular oxygen via chemical reaction.[7] Numerous techniques have been implemented to develop brand new electrocatalysts for OER to enhance the efficiency of gas evolution.

In fact, OER is a four electron-proton coupled anodic reaction, which means it demands higher energy to overpowers kinetic barrier to deliver appreciable current. The OER reaction has sluggish kinetics like ORR, thus, a catalyst should be designed to proceed the reaction at lower potential.[8] Moreover, the OER reaction is highly pH-dependent and generate different products under various electrolyte environments as shown below:[9]

In alkaline solution:[9]

$4\ OH^- \leftrightarrow 2\ H_2O_{(l)} + O_{2(g)} + 4\ e^-$ $\qquad E^0_a = 0.404$ V

In acidic solution:[9]

$2\ H_2O_{(l)} \leftrightarrow 4\ H^+ + O_{2(g)} + 4\ e^-$ $\qquad E^0_a = 1.23$ V

The transition metals such as Ru and Ir were regarded as state-of-the-art catalysts for OER due to their superior stability, low overpotential and Tafel slope. It was experimentally proved that electrocatalytic activity of nanoparticle catalysts towards the OER decline in the sequence of Ru>Ir>Pt. According to recent investigations, activity decreases as $Ru > Ir \approx RuO_2 > IrO_2$, but dissolution of catalysts soars as $IrO_2 \ll RuO_2 < Ir \ll Ru$. However, these metals show 2-3 orders of magnitude greater than their respective oxides when they dissolve either in alkaline or acidic medium.[9]

Currently, the noble metal-based IrO_2 and RuO_2 catalysts are regarded as benchmark electrocatalysts for OER due to high potential applied in the electrode, as well as their high electrocatalytic performance towards the OER in both acidic and alkaline solution. However, IrO_2 promises more advantage than RuO_2 for having ability to be sustainable at higher anodic potential in both alkaline and harsh acidic media.[10] According to these facts, various strategies can be mapped out to prepare desirable electrocatalyst for OER such as having high electrical conductivity to deliver charge-carriers from the metal electrode to adsorbed intermediates. Diverse perspectives can be implemented, for instance, blend with conductive material, introducing foreign elements and altering morphology to enhance not only conductivity, but also catalytic ability. Moreover, phase degradation of electrocatalyst should be prevented at high anodic potential in redox reactions since electrocatalyst can dissolve in electrolyte or slowly strip from the electrode in case of phase transformation during the OER process. For the purpose of both prolong lifetime and enhance stability of electrocatalysts, it should comprise other elements (mixing Ir into RuO_2 to form $Ru_xIr_{1-x}O_2$).[8]

In last few decades, extensive studies have been conducted to develop electrocatalysts for OER applications. Among several materials, CoO_x got great attention because of its mixed oxidation states of $Co^{2+/3+/4+}$. Besides, phase transformation of Co-based materials, for instance, oxides to oxyhydroxides or hydroxides play a dynamic role during the OER reaction. It was found that morphology, surface area and oxidation state effect the activity of Co_3O_4. Oxygen vacancy was created on surface of mesoporous Co_3O_4 nanowires by reduction method, since nanowire structures are quite desirable for charge transfer, while mesoporous structure promote more active sites. Furthermore, presence of oxygen vacancies improve the electrical conductivity as a result of establishment of novel states by delocalization of the Co-O bonds which leads to increased activity of the mesoporous Co_3O_4 nanowires towards the OER. Additionally, the surface energy is crucial point that drives reactivity. The surface energy for NiO facets change in the sequence of {101}>{113}>{100}, where the {101} facets are recommended for OER procedure. It was analyzed that {101} facets of NiO nanosheet stimulated by TiO_2 performs superior OER performance in alkaline media. Moreover, altering electronic structure and intermediate bonds enhance electrical conductivity along with OER activity of NiO in case of alloying it with some metals including Fe and Co. However, materials with complex 3D, porous and hollow structures have capacity to display brilliant OER activity. For example, mixture of 3D hierarchical structure with 1D nanowire mesh yields $NiCo_2O_4$ hollow microcuboids which provides even path for the electrolyte to pass through and enough contact area between reactants and active site.

Alternatively, Co_2B has been fabricated via chemical reaction of $CoCl_2$ with $NaBH_4$ and exhibit enhanced OER activity than benchmark catalysts in alkaline solution. On the other hand, annealing temperature also lead to outstanding performance, since either desirable conductivity or crystal structures were observed when material annealed at 500 °C.

All in all, there have been many experiments conducted in the field of OER electrocatalysis, but still it is challenging to make it available at industrial scale for hydrogen production from water electrolysis and for metal-air batteries in favor to reduce consumption of fossil fuel energy.[9]

2.3. Bifunctional ORR/OER catalysts

The oxygen electrocatalysis, namely the oxygen reduction and evolution reactions, is conventionally carried out by employing noble metal and metal oxide-based materials. Although they have some drawbacks such as high price, harmful environmental consequences and lower permanence/selectivity. Both reactions require distinctive conditions, specifically the electric potentials shrink the number of materials that catalyze ORR/OER and bring in more restraining factors that can hinder catalytic activity. For instance, Pt-based materials are the state-of-the-art ORR catalysts, yet not effective towards the OER, because of the evolution of Pt oxides on the surface of catalyst at high anodic potentials. Besides, the assembly of working electrode applying two non-identical materials for sole ORR or OER, cause cost-push inflation and introduces fabrication problems.[11]

The common way of determining a promising bifunctional catalyst towards the ORR and OER is by considering its overpotential at a specified current density along with same catalyst loading. The efficient bifunctional catalyst shows slighter overpotential at a given rate. However, it is important to produce a bifunctional catalyst, which is capable of tolerating harsh environments occurred during the ORR and OER, albeit still displaying remarkable activity.[11]

The transition metal (Mn, Co, Ni, Fe) oxides have considered as good bifunctional ORR/OER catalysts because of their adequate stability and intrinsic electrocatalytic activity in oxidative electrochemical environments.

Moreover, the electrical conductivity and electron density of materials rise due to the oxygen vacancies (OVs), which play role of donors to reduce the bandgap. Also, the surface OVs can improve the electron transfer between O-vacancies and metal d-band to regulate the adsorption of surface species toward catalysis. Furthermore, OV-containing oxide exhibits lesser peroxide

production, increased positive potential, higher current for ORR electrocatalysis, and also aid OER electrocatalysis. The contact through oxygen-containing species and catalyst surface enhances because of presence of OVs which minimize the reaction kinetic barrier.

The other group of substances known as spinel oxides ($A_xB_{3-x}O_4$) can be utilized as bifunctional ORR/OER catalyst in alkaline electrolyte. Because the electron transfer takes place between the cations of unlike valences with slightly low activation energy amid spinel oxides. Likewise, perovskite oxides (ABO_3) are extensively explored as bifunctional ORR/OER catalyst in alkaline media, too. The A and B can be partially replaced with different metal components, which can finely adjust either their compositions or properties. Generally, A-site has effect on oxygen adsorption, and the activity of the adsorbed oxygen is prompted by B-site.[11] By co-doping with nitrogen and phosphorus the mesoporous carbon foam shows an excellent bifunctional electrocatalytic activity for ORR and OER. Besides, cobalt-embedded carbon/nanodiamond electrocatalyst that doped with nitrogen performed well towards ORR/OER in alkaline condition.[12]

To design good bifunctional PGM-free catalysts, the specific type of porous coordination polymers, which is called metal-organic frameworks (MOFs) are propitious precursors. Typically, MOF composited with metal centers bridged by organic ligands and selection of ligands along with coordination nature of metal influence the quantity of ligands join metal and orientation, hence greatly altering the shape and pores size of the MOF.

Evidently, the morphology of MOF precursors can be tuned by pyrolyzing the MOFs, i.e. MOF-derived catalysts and changing the MOF precursors can enhance the composition of MOF-derived catalysts. Besides, carbon skeleton in MOF-derived catalysts supplies ceaseless electron transfer pathways and distinct porous feature of MOF sustain good templates to set up mass transfer channels. Furthermore, the noble-metal-free catalysts for ORR/OER requisite transition metals (Fe, Co, Ni, etc.). The transition metals possess partly filled d orbitals that hybridize and cause diverse yet controllable coordination geometries by employing MOF precursors. As a result of superior electronic conductivity and inimitable functions to sturdy ORR/OER kinetics, carbon skeleton is imperative, notwithstanding the real active sited of the PGM-free catalysts is the subject of the debate.[13]

For instance, the TM-N_x moieties that are embodied in the carbon matrix are assumed as active sites in single atom TM-N-C catalysts. It is worth mentioning that carbon matrix stabilizes the TM-N_x moieties as well as maintain the electron transfer channels during the ORR and OER. There are several kinds of MOF-derived catalysts such as metal-free heteroatom-doped carbon materials, single-atom TM-N-C catalysts, TM-based particle decorated carbon materials as

well. Generally, the single-atom TM-N_x moieties (TM = Fe, Co, Mn, Cu, etc.) are the active sites for ORR and in order to design well-defined TM-N_x moieties to prevent aggregations of TM elements, not only TM contents, but also size distribution should be taken into consideration as primary factors in MOF precursors.

Overall, the model MOF precursors are needed to explore active sites and coherent construction the MOF-derived TM@C type catalysts.[13]

3. AIMS OF THE THESIS

- The main focuses of this thesis are:
- The synthesis of TAL-2-based Co-N-C electrocatalytic material.
- Demonstration of an optimized post-synthetic treatment of TAL-2-based catalyst materials.
- To explore surface morphology of the electrocatalytic materials.
- The study of the ORR/OER electrocatalytic activity of the optimized catalyst materials.
- The comparison of the electrocatalytic activity of TAL-2-based catalysts treated at different post-synthetic conditions.
- To establish a link between the catalytic mechanism by morphology and electrochemical behavior results.

4. EXPERIMENTAL PART

4.1. Materials and reagents

The four different acid solutions were prepared for acid treatment of carbonized TAL-2 derived catalyst material. To be specific, calculated amount of nitric acid (HNO_3), sulfuric acid (H_2SO_4) and hydrochloric acid (HCl) were diluted separately with Milli-Q water (Millipore, Inc.) to prepare 0.5 M solution along with mixture of diluted 0.5 M nitric and sulfuric acid solution, all prepared solutions labelled as L1, L2, L3, L4, respectively, too. Besides, 3.3 g of KOH pellets (purity ≥85%, Sigma-Aldrich) was dissolved in Milli-Q water to make 0.1 M electrolyte solution which was saturated with O_2 (99.999%, Linde Gas) and deaerated by purging with Ar (99.999%, Linde Gas) to carry out electrochemical experiments. The catalyst ink was made by using perfluorinated resin solution containing Nafion (5 wt%, Sigma-Aldrich) and 2-propanol.

4.2. Synthesis of TAL2-based materials

The 25% aq. ammonia (NH_3), dimethylformamide ($(CH_3)_2NCH$), ethanol (C_2H_5OH) and water (H_2O) were prepared in 4:10:10:15 ratio to mix with 33.30 mmol of 1H-benzo[d]imidazole-5,6-diol and 16.64 mmol of cobalt(II) chloride hexahydrate ($CoCl_2 \cdot 6H_2O$) was added drop by drop to this mixture (Fig. 2). The final solution was abandoned to stir at room temperature for a day and then it was filtered, washed with ethanol, as well as dried to obtain TAL-2 catalyst material whose color was dark green. The collected catalyst material was pyrolyzed at optimized temperature of 700, 800, 900, 1000 °C using a small tube furnace (EST 12/300B, Carbolite Ltd.) under N_2 (99.999%, Linde Gas) flow for 2h (rapid heating, rapid cooling). The resulting pyrolyzed materials from different temperatures were divided into 3 groups (B1, B2, B3) for further processes as illustrated in Scheme 1.

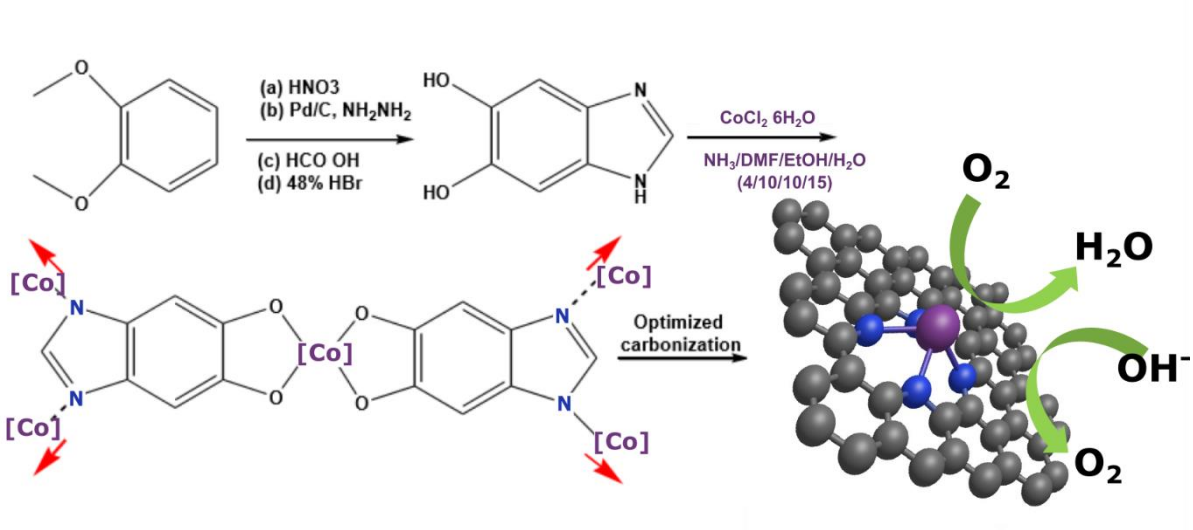

Figure 2. Synthesis of TAL-2 based material

Acid treatment was applied for first and second group (B1, B2) carbonized materials by suspending them in four various 0.5 M acid solutions, i.e., nitric acid (L1), sulfuric acid (L2), hydrochloric acid (L3), mixture of nitric acid and sulfuric acid (L4) solutions, stirred for 5 h at 80 °C and 8 h at 50 °C with respect to their group numbers, filtered, recarbonized under an inert atmosphere (N_2 flow) at the same temperature and time (2 h) to get final TAL-2 derived catalyst material. Third group of catalysts B3 was left out of acid leaching and was intended to use during comparative analyses.

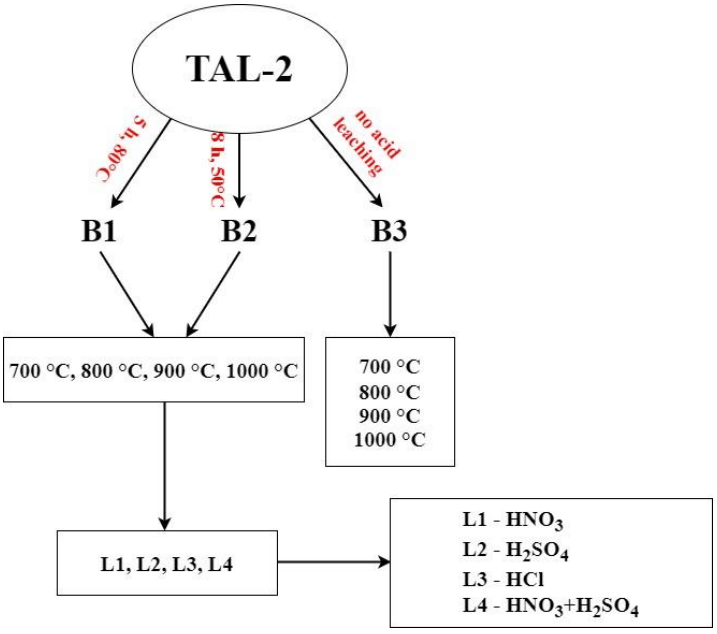

Scheme 1. Illustration of sample groups

4.3. Morphological characterization

The morphology and microstructure of all 36 TAL-2-based samples was examined by scanning electron microscopy (SEM) measurements, which were performed using Zeiss Ultra–55. Prior SEM measurements ample powder was deposited onto the carbon tape.

Prior to BET measurements, the catalysts were vacuum-dried overnight at 200 °C. The BET analysis was performed using NovaTouch LX2 instrument (Quantachrome) at the boiling point of nitrogen (77 K). Specific surface area (S_{BET}) values were calculated using the Brunauer-Emmett-Teller theory. All of the calculations were performed using TouchWin 1.11 software (Quantachrome Instruments).

The surface composition of samples was studied using X-ray photoelectron spectroscopy (XPS). Measurements were done at ultra-high vacuum conditions using a non-monochromatic twin anode X-ray tube (Thermo XR3E2) with the energy of 1253.6 eV (Mg K_α) and an electron energy analyzer SCIENTA SES 100. The data was processed with CasaXPS (version 2.3.17). Gauss–Lorentz hybrid function (GL 70, Gauss 30%, Lorentz 70%) and blend of linear and Shirley-type backgrounds were used for fitting the peaks.

Powder X-ray diffraction (PXRD) studies were done on Bruker D8 Advance diffractometer with Ni filtered Cu Kα radiation. The diffraction patterns were obtained with scanning steps of 0.0126° 2θ in the range of 5° to 89° and the counting time of 525 s per step. The content of components and the size of crystallites were quantified using Bruker's Topas 6 software.

Raman spectra were recorded on Horiba's LabRam HR800 spectrometer with a laser line of 532 nm, which was focused on the sample with a spot size of 5 μm.

4.4. Electrochemical characterization

The electrochemical measurements were performed in a three-electrode electrochemical cell. The glassy carbon (GC) rod was used as a counter electrode, which was isolated in a fritted compartment. Reversible hydrogen electrode (RHE) was used as a reference electrode isolated from the working solution using a Luggin capillary and the working electrode was a glassy carbon electrode with diameter of 5 mm mounted into a Teflon holder. In advance of modification, glassy carbon disk electrodes were polished with alumina slurries (1 and 0.3 μm,

Buehler). Moreover, the electrodes were sonicated in both Milli-Q water and isopropanol to clear away polishing residue in an ultrasonic bath for 5 min.

The catalyst ink was obtained by preparing mixture of 5 mg of electrocatalyst material, 0.495 ml of 2-propanol and 5 µl of Nafion solution (5 wt%) in an ultrasonic bath. 10 µl of the catalyst suspension was deposited onto surface of a clean GC. The catalyst loading was 0.50 mg cm^{-2}.

The rotating disc electrode (RDE) method was employed to study the electrocatalytic activity of the catalysts towards the ORR and cyclic voltammograms were examined at a potential sweep rate (v) of 50 mV s^{-1} in Ar-saturated electrolyte solution in the potential range of -0.2÷1.1 V. The ORR polarization curves were measured in O_2-saturated 0.1 M KOH solution at a scan rate of 10 mV s^{-1} in the potential range of -0.2÷1.1 V at varied electrode rotation rates (ω): 360-3100 rpm. The rotation speed of electrode was managed using a CTV101 speed control unit joined to an EDI101 rotator (Radiometer). Background currents were assessed in Ar-saturated solution at a scan rate of 10 mV s^{-1} in the potential range of -0.2÷1.1 V. The background correction was done by subtracting background currents from the RDE data and data was normalized to the geometric area of the GC electrode. The data of ORR and OER were automatically corrected for i*R* drop employing Nova 2.1.4 software. The Electrochemical Impedance Spectroscopy (EIS) was utilized to determine the R value, which was in the range of 40-50 Ω for TAL-2 modified glassy carbon electrodes in 0.1 M KOH solution.

Koutecky−Levich (K–L) plots at different electrode potentials were extracted from the RDE data. The number of electrons transferred per O_2 molecule (*n*) was calculated from the RDE data using the K–L equation:[14]

$$\frac{\mathbf{1}}{\boldsymbol{j}} = \frac{\mathbf{1}}{\boldsymbol{j_k}} + \frac{\mathbf{1}}{\boldsymbol{j_d}} = -\frac{\mathbf{1}}{\boldsymbol{nFkC_{O_2}^b}} - \frac{\mathbf{1}}{\mathbf{0.62}\boldsymbol{nFD_{O_2}^{2/3}\nu^{-1/6}C_{O_2}^b\omega^{1/2}}} \quad (1)$$

where *j* indicates the measured current density at a specific potential, j_k and j_d are the kinetic and diffusion limited current densities, respectively. *n* is transferred electron number, *F* is the Faraday constant (96 485 C mol^{-1}), *k* denotes rate constant for electrochemical reduction of oxygen, $\boldsymbol{C_{O_2}^b}$ represents the concentration of O_2 (1.22×10^{-6} mol cm^{-3} in 0.1 M KOH),[14] while $\boldsymbol{D_{O_2}}$ is the diffusion coefficient of O_2 (1.93×10^{-5} cm^2 s^{-1} in 0.1 M KOH),[14] *v* denotes the kinematic viscosity of the solution (0.01 cm^2 s^{-1})[14] and *ω* indicates the rotation rate of the electrode (rad s^{-1}).

5. RESULTS AND DISCUSSION

5.1. Surface structure of TAL-2-based catalysts

Surface morphology and microstructure of TAL-2 precursor and post-synthetically treated TAL-2-based materials was examined by SEM technique. The scanning electron microscopy images of the TAL-2 derived materials display almost similar morphology (Fig. 3). Thus, the SEM image also clearly verified the highly porous nature of carbon matrix, in which abundant mesopores can be observed.

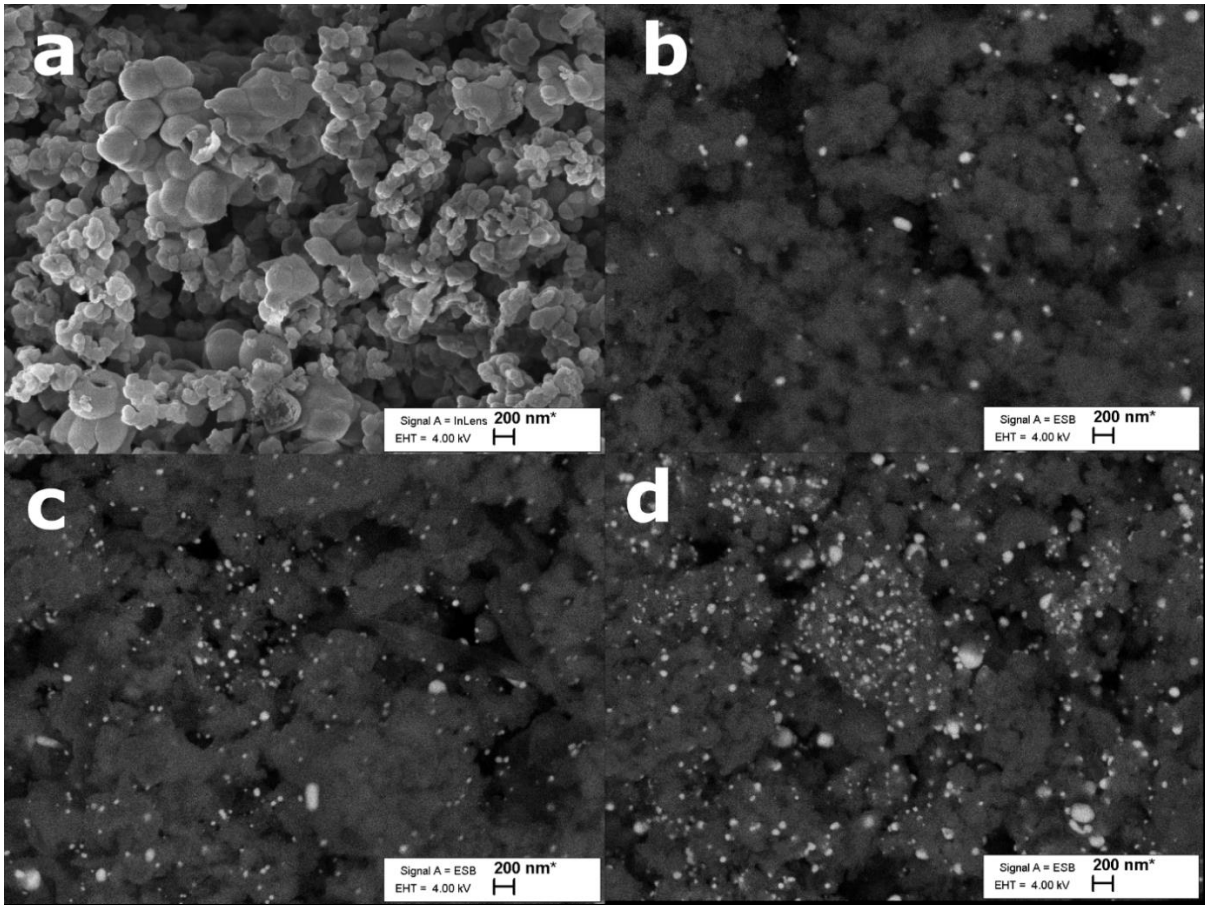

Figure 3. SEM micrographs of (a) uncarbonized TAL-2 precursor and TAL2-based catalysts carbonized at (b) 800L1B2, (c) 900L3B1 and (d) 1000L3B1, respectively.

The N_2 adsorption/desorption isotherm of the catalysts was performed using a physicochemical adsorption instrument, and the specific surface area and pore size distribution of the materials were calculated using the Brunauer-Emmett-Teller, and Density Functional Theory (DFT) methods. Throughout the series, BET surface area for the TAL-2-based catalyst materials have diverse values (Fig. 4a) along with total and microporous volume of pores (Fig. 4b) distributed

in the materials. According to the result of BET measurement, the four samples of B3 group which have not gone through acid leaching exhibited lower specific surface area in the range of 300-500 $m^2\ g^{-1}$ with the total pore volume between 0.3 and 0.5 $cm^3\ g^{-1}$. However, the catalyst materials, which belong to B1 group have higher specific surface area ranging from 700 to 950 $m^2\ g^{-1}$ (V_{tot}: 0.7-1.1 $cm^3\ g^{-1}$). The BET surface area changes between 500-650 $m^2\ g^{-1}$ (V_{tot}: 0.4-0.7 $cm^3\ g^{-1}$) for the samples whose acid leaching have been carried out at 50 °C during 8 h. Besides, the scope of the microporous volume of TAL-2-based catalyst materials was 0.1-0.3 $cm^3\ g^{-1}$ (Fig. 4b). Overall, larger specific surface area and highly porous structure are contributed to expose catalytic active sites to improve diffusion pathways for reactants.

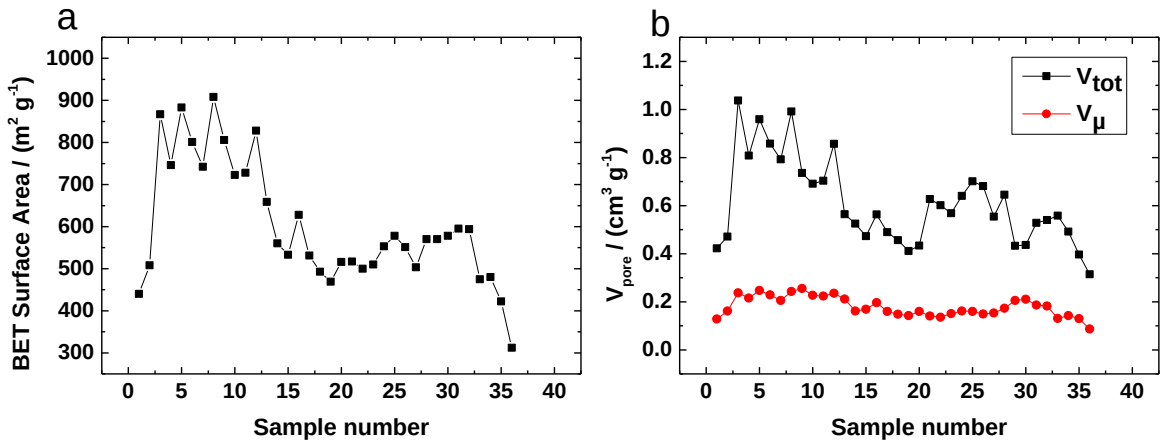

Figure 4. The obtained (a) BET surface area ($m^2\ g^{-1}$) (b) V_{tot} and V_{μ} are total and microporous volume determined using the DFT calculation for different TAL-2 based catalysts.

To investigate surface structure of TAL-2-based materials all 36 samples prepared in this work were analyzed by powder X-ray diffraction spectroscopy. According to a qualitative analysis of the PXRD data, the samples can be grouped based on both their temperatures and treatment. The XRD diffraction lines are presented in Fig. 5 for 4 different temperature groups.

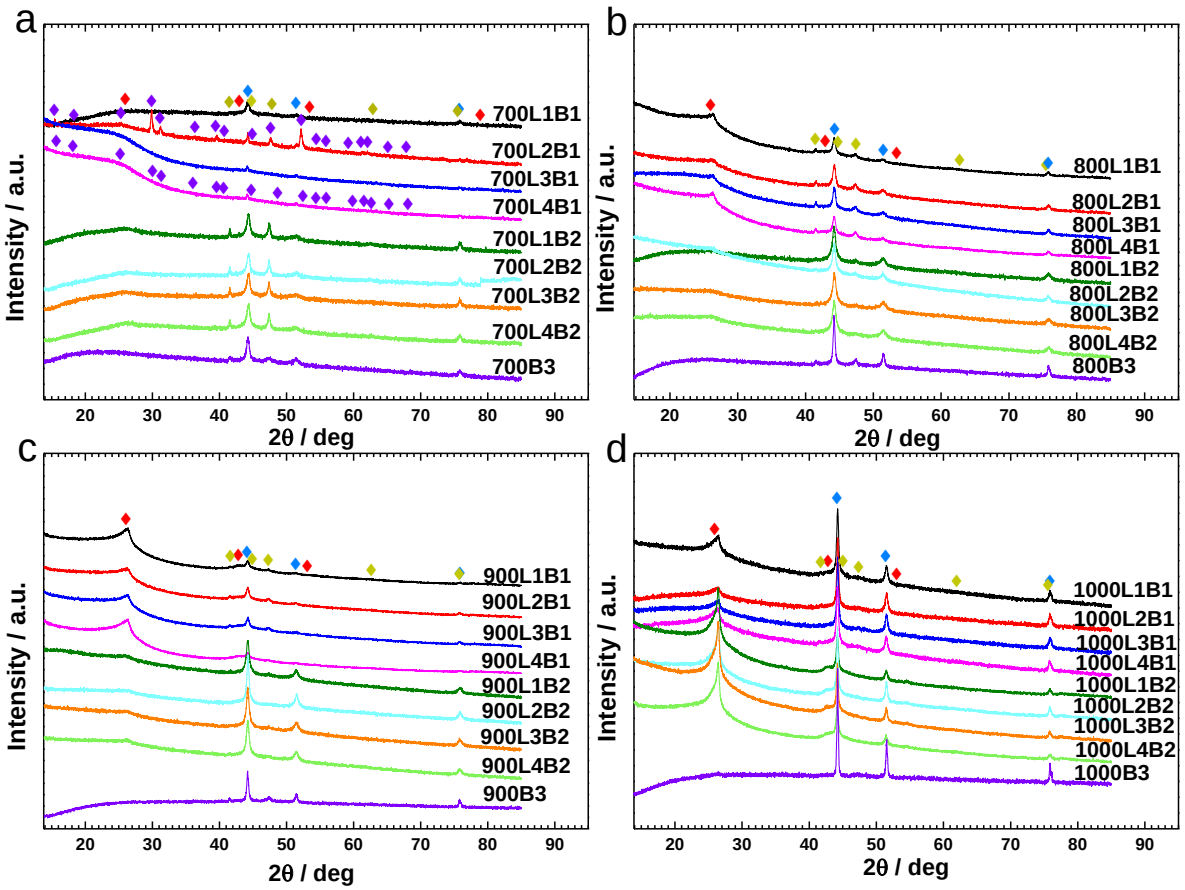

Figure 5. PXRD patterns of all TAL2-based catalysts: ♦ C Hexagonal (PDF 00_058_1638); ♦ Co Cubic (PDF 00_015_0806); ♦ Co Hexagonal (PDF 04_001_3273); ♦ Co_9S_8 Cubic (PDF 00_056_0002).

The following can be distinguished in the samples in agreement with their crystal structure: 1) carbon with different structural arrangements, 2) cubic cobalt, 3) hexagonal cobalt and 4) cobalt sulfide or cobalt pentlandite (Co_9S_8) in two samples.

As a general trend, carbon graphite and the proportion of cubic cobalt and the size of crystallites increase with increasing temperature (Table 1). At the same time, the content of hexagonal cobalt decreases with increasing temperature. There are differences in these general regularities between treatments. Changes in mineral composition are more grouped by treatments B1 and B2. To describe carbon, three graphite models with different crystallite sizes and elementary cell sizes were employed. The names of these components are conditional. "Amorphous graphite" is not amorphous in the physical sense, but fine carbon with chemically unbound layers. "Coarse graphite" is defined in the model as > = 10 nm and > = 20 nm at 1000 °C.

The content of hexagonal cobalt is higher in B1 treatments, decreasing with increasing temperature. As the temperature increases, the size and structural order of the hexagonal cobalt crystallites decrease. The size of cubic cobalt crystallites increases with increasing temperature. Its contents are higher in B2 treatments, except at 1000 °C. Cobalt sulfide was found in samples

TAL-2-700L2B1, TAL-2-700L4B1. All samples were measured on a Si single crystal low background sample holder that did not yield additional peaks.

Table 1. Crystallite size of various species in TAL-2-based catalyst materials (nm)

N	Sample	Phase name and crystallite size					
		Graphite 2H am	Cobalt_C	Cobalt_H	Graphite coarse	Graphite 2H	Cobaltpentlandite, syn
1	TAL2@700L1B1	0.9±0	23.3±2.1	23.8±18.8	10±3.6	6.7±0.2	
2	TAL2@700L2B1	0.9±0	67.2±6.6		10±4.2	6.7±0.2	40±0.9
3	TAL2@700L3B1	0.9±0	65.1±9.3				
4	TAL2@700L4B1	0.9±0	21.2±1.3	15±4.4			41.3±5.2
5	TAL2@800L1B1	0.9±0	34.9±2	17.9±1	10±0.4	6.7±0.2	
6	TAL2@800L2B1	0.9±0	28.1±1.3	15.4±0.6	10±0.8	6.7±0.2	
7	TAL2@800L3B1	0.9±0	29.8±0.9	23.1±1.3	14.2±1.3	6.7±.02	
8	TAL2@800L4B1	0.9±0	35.5±1.4	33.5±2.3	10±0.5	6.7±0.2	
9	TAL2@900L1B1	0.9±0	52.4±7.8	15±0.9	10±0.3	6.7±0.2	
10	TAL2@900L2B1	0.9±0	35.2±1.9	21.9±1.5	10±0.4	6.7±0.2	
11	TAL2@900L3B1	0.9±0	36.6±2.3	13.9±0.8	10±0.4	6.7±0.2	
12	TAL2@900L4B1	0.9±0	83.3±27	49.2±16.6	10±0.3	6.7±0.2	
13	TAL2@1000L1B1	0.9±0	38.3±0.9	15±0.9	10±0.3	6.7±0.2	
14	TAL2@1000L2B1	0.9±0	41.4±1	15±0.9	10±0.7	6.7±0.2	
15	TAL2@1000L3B1	0.9±0	40.2±1	15±0.9	10±0.6	6.7±0.2	
16	TAL2@1000L4B1	0.9±0	37.7±1.1	15±0.9	10±0.4	6.7±0.2	
17	TAL2@700L1B2	0.9±0	19.4±0.7	33.9±2.2			
18	TAL2@700L2B2	0.9±0	22.3±0.9	38.9±2.8			
19	TAL2@700L3B2	0.9±0	17.8±0.6	33.6±1.5			
20	TAL2@700L4B2	0.9±0	18.2±0.7	34.8±2.6	10±1.3	6.7±0.2	
21	TAL2@800L1B2	0.9±0	15.7±0.6	20±0.8			
22	TAL2@800L2B2	0.9±0	17±0.4	15±1.2	10±1.9	6.7±0.2	
23	TAL2@800L3B2	0.9±0	14.5±0.2	15±2	10±2.4	6.7±0.2	
24	TAL2@800L4B2	0.9±0	15.5±0.4	15±2.9	10±1.8	6.7±0.2	
25	TAL2@900L1B2	0.9±0	18.2±0.3	20±0.8		6.7±0.2	
26	TAL2@900L2B2	0.9±0	26.3±0.3	20±0.8		6.7±0.2	
27	TAL2@900L3B2	0.9±0	19.5±0.2	20±0.8		6.7±0.2	
28	TAL2@900L4B2	0.9±0	20±0.4	20±0.8	10±1.2	6.7±0.2	
29	TAL2@1000L1B2	0.9±0	64.2±2.5		20±0	6.7±0.2	
30	TAL2@1000L2B2	0.9±0	73.9±1.9		20±0	6.7±0.2	
31	TAL2@1000L3B2	0.9±0	78.5±2.9		20±0	6.7±0.2	
32	TAL2@1000L4B2	0.9±0	50.5±1.7		20±0	6.7±0.2	
33	TAL2@700B3	0.9±0	24.9±1.6	15.6±1.5			
34	TAL2@800B3	0.9±0	52.8±2.8	48.5±10.6			
35	TAL2@900B3	0.9±0	56.4±4.2	15±0.9		6.7±0.2	
36	TAL2@1000B3	0.9±0	144.5±6.6	15±0.9	10±4.9	6.7±0.2	

To characterize the changes in structure of the samples Raman tests were performed. Typical D and G peaks appearing near 1330 cm^{-1} and 1580 cm^{-1} were obtained, which are related to the disordered/defective structure of carbon and the ordered graphitic carbon structure, respectively.[15] The I_D/I_G ratios are given in the Fig. 6 in the range of 1.70–2.25. It is apparent

that TAL-2-800L4B2 shows relatively higher I_D/I_G ratio compared to other counterparts, which emphasize greater structural defects.

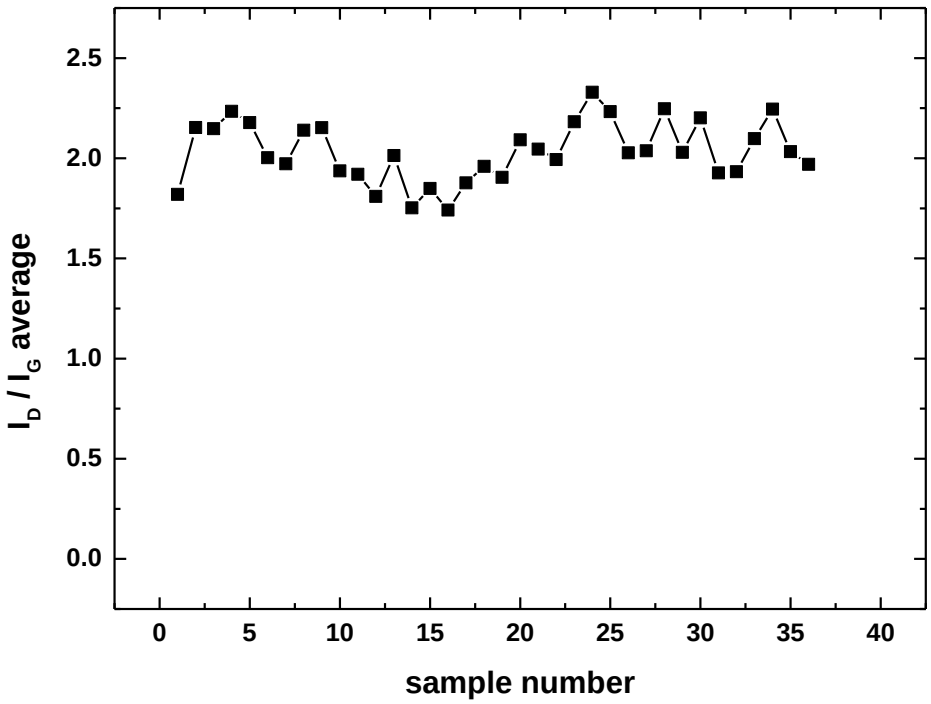

Figure 6. The average I_D/I_G ratio for various TAL-2 based electrocatalyst materials.

The total elemental composition of the catalyst surface was examined by XPS analysis (Fig. 7) verifying the C, N, Co, O elements in the samples. As can be seen from Fig. 7, the carbon content increased by increasing of carbonization temperature. Alongside with increasing carbonization temperature, a reduction in the nitrogen content can be observed. The highest amount of nitrogen was observed in samples of 700B1 series and TAL-2-800B3. It is interesting that the average amount of cobalt on the surface of B1 is almost constant and changes with the changing in leaching procedure (B2 and B3). Evidently, the amount of Co3p is lowest (0.62%) in the B1 group samples, which have gone through acid treatment (5 h, 80 °C) and second step pyrolysis, compared to only one step pyrolyzed samples of B3 group (2.2%). Additionally, amount of O1s species is lower in B1 group catalyst materials than that of B3 group materials with 5.27 and 5.55%, respectively.

However, content of carbon is higher (87.37%) in samples whose acid leaching was conducted at 80 °C for 5 h rather than samples of B3 group (85.43%) which carbonized only once.

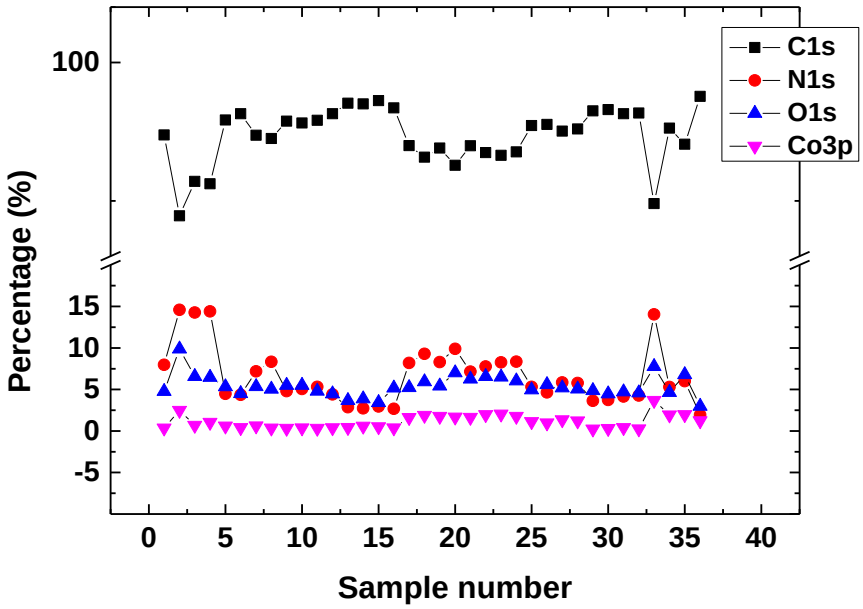

Figure 7. Surface elemental composition of TAL2-based catalysts obtained from XPS analysis (at.%).

The relative concentration of each four species are described in Fig. 8. According to Fig. 8a, TAL-2-1000B3 showed highest amount of C1s_sp2 (78.99%). The average contribution of components of C1s (excl. C1s_sp2 and C1s_sp3) was in the range of 1.22-5.32% through all samples. It is clearly seen that N1s_pyridinic exhibit highest concentration in TAL-2-700B3 which was followed by B1 group catalysts. The amount of both N1s_graphitic and N1s_oxidic was up to 0.6% (Fig. 8b). Fig. 8c provides information about amount of O1s species where TAL-2-700L2B1 and TAL-2-700B3 possess highest quantity of O1s_OH_C=O with 5.01% and 4.11%, respectively. However, the trend is opposite towards Co3p_2+ in these two samples (TAL-2-B3: 1.693%, TAL-2-700L2B1: 1.314%) (Fig. 8d).

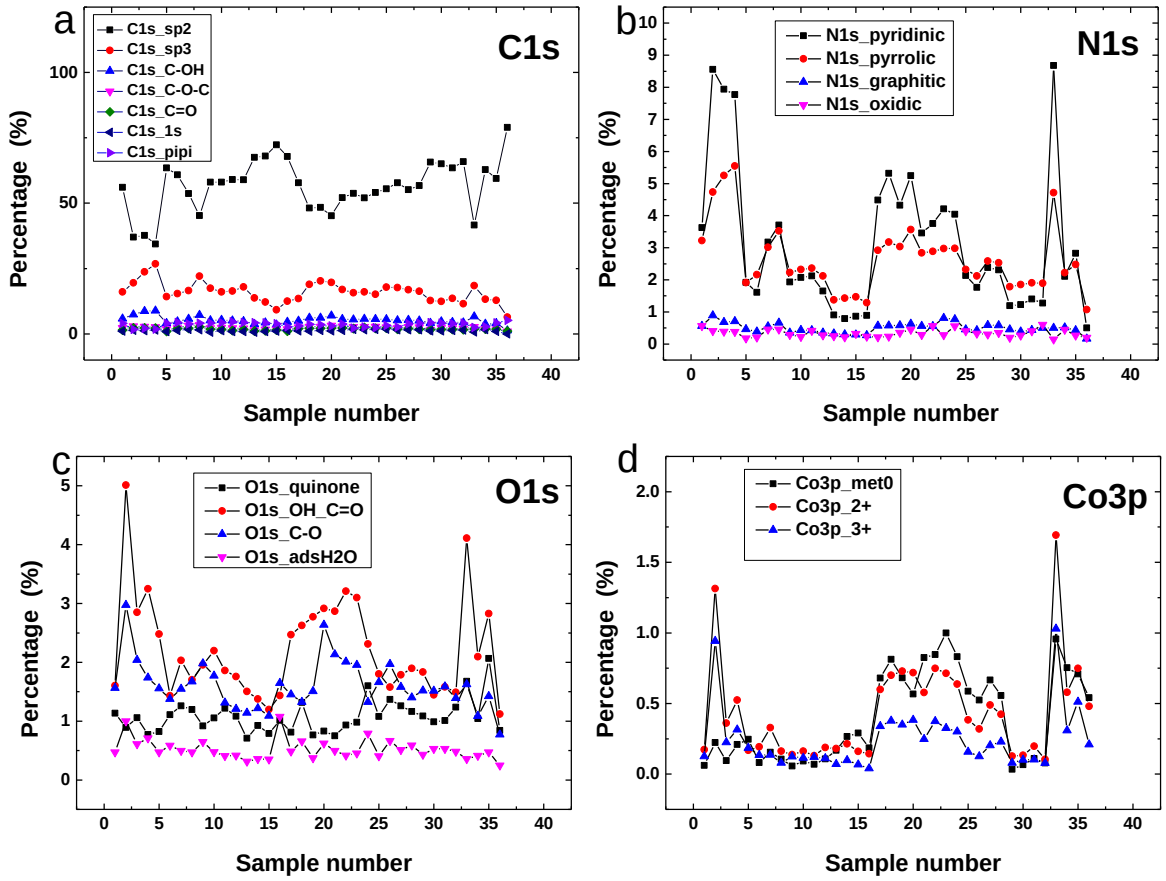

Figure 8. Relative concentration of (a) carbon, (b) nitrogen, (c) oxygen and (d) cobalt species in TAL2-based Co-N-C materials.

5.2. Electrochemical measurements

5.2.1. Cyclic voltammetry

Cyclic voltammetry is a straightforward yet effective method of electrochemical analysis which used to get information about charge-transfer behavior at an electrode-electrolyte interface in a particular potential range. It measures the current, which is induced by an electrochemical cell as a function of applied potential.[16]

The electrochemical responses of TAL-2 samples were also investigated in a three-electrode cell via cyclic voltammetry (CV) in 0.1 M KOH electrolyte solution, which was saturated with Ar. The potential of the working electrode was scanned back and forth at a constant scan rate of 50 mV s^{-1} in a potential window of -0.2÷1.1 V for several cycles. The resulted current values were normalized to the geometric surface area of the GC electrode and the obtained current density values were plotted versus potential (Fig. 9).

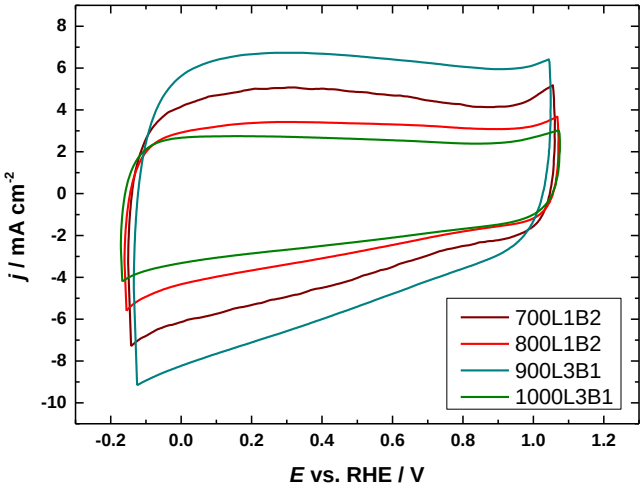

Figure 9. CV curves of TAL-2-700L1B2, TAL-2-800L1B2, TAL- 2-900L3B1 and TAL-2-1000L3B1 samples in Ar-saturated 0.1 M KOH

5.2.2. ORR studies

The series of catalysts were developed from an amorphous metal-organic framework (MOF) precursor TAL-2 by heat treatment it at various temperatures and acid leaching was applied to majority of them (Group 1 and 2 catalysts) in this work. The obtained catalysts materials together with raw counterparts were screened as bifunctional electrocatalyst materials for oxygen reduction reaction (ORR) and oxygen evolution reaction (OER). To gain understanding of effect of divergent pyrolysis temperatures on the electrocatalytic performance of TAL-2 based catalysts toward the ORR, the rotating disc electrode (RDE) technique was employed in 0.1 M KOH electrolyte. Oxygen reduction polarization curves (Fig. 10a) validated that TAL-2 based catalyst carbonized at 800 °C (TAL-2-800L1B2) had the highest ORR electrocatalytic activity with an onset potential (E_{on}) of 0.949 V, a half-wave potential ($E_{1/2}$) of 0.862 V, which is close to the kinetic parameters of other promising non-noble metal ORR catalysts (Table 3).

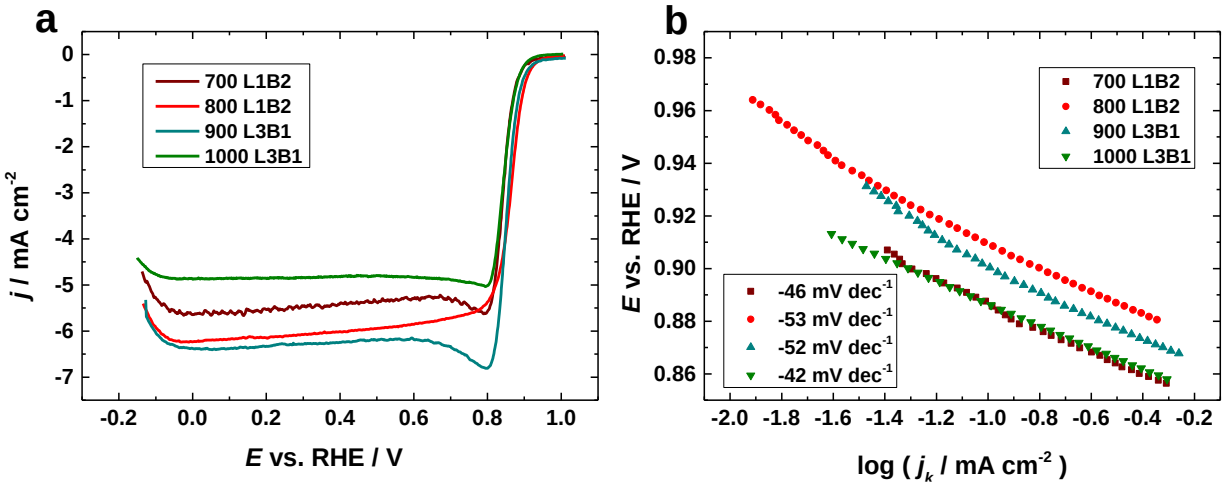

Figure 10. (a) ORR polarization curves for TAL-2-700L1B2, TAL-2-800L1B2, TAL-2-900L3B1 and TAL-2-1000L3B1 catalyst materials in O_2-saturated 0.1 M KOH. (b) Tafel plots for ORR on TAL-2-700L1B2, TAL-2-800L1B2, TAL-2-900L3B1 and TAL-2-1000L3B1.

The Koutecky-Levich (K-L) plots were set up using data derived from RDE and calculated electron transfer numbers by using the K-L equation (1) were approximately equal to four in the potential range -0.1÷0.7 V (Fig. 11) in all cases which is considered as a favorable result.

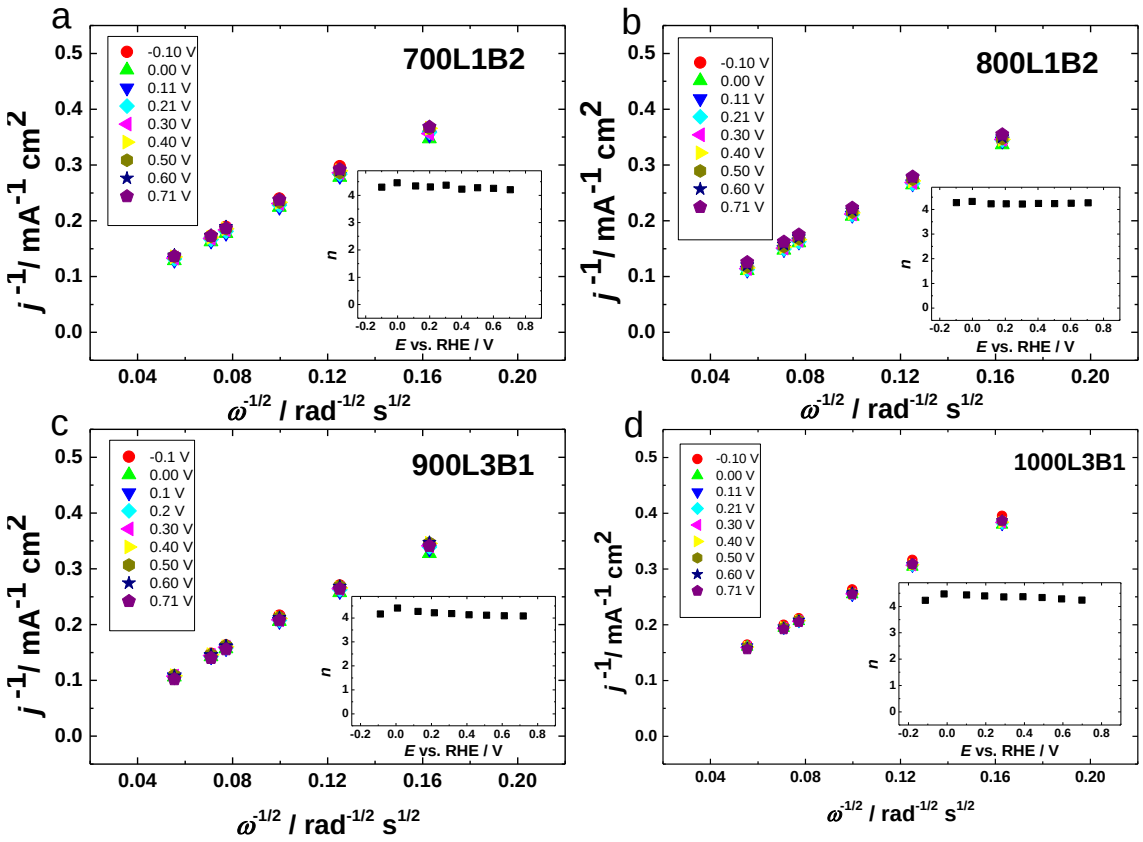

Figure 11. Koutecky–Levich plots for O2 reduction on TAL-2-700L1B2, TAL-2-800L1B2, TAL-2-900L3B1 and TAL-2-1000L3B1 modified GC electrodes; insets: numbers of electrons transferred per O2 molecule.

5.2.3. OER studies

The OER catalytic activities are then assessed in 0.1 M KOH and i*R*-corrected polarization curves at a scan rate of 10 mV s^{-1} are recorded in Fig. 12a. The benchmark current density of 10 mA cm^{-2} was accomplished at 1.56 V for TAL-2-900L1B2 material. For further understanding the overall oxygen electrode activity as bifunctional O_2 catalysts, calculation of subtraction (ΔE) of OER ($E_{j=10}$) and ORR ($E_{1/2}$) metrics was done, where the smaller ΔE, the superior towards O_2 electrode. Evidently, TAL-2-700L1B2 shows a ΔE of 0.736 V ($E_{j=10}$ =

1.58 V; $E_{1/2}$ = 0.844 V), which makes it lower than the rest of the TAL-2 catalyst samples of this work and close to other non-precious metal bifunctional catalysts (Table 3).

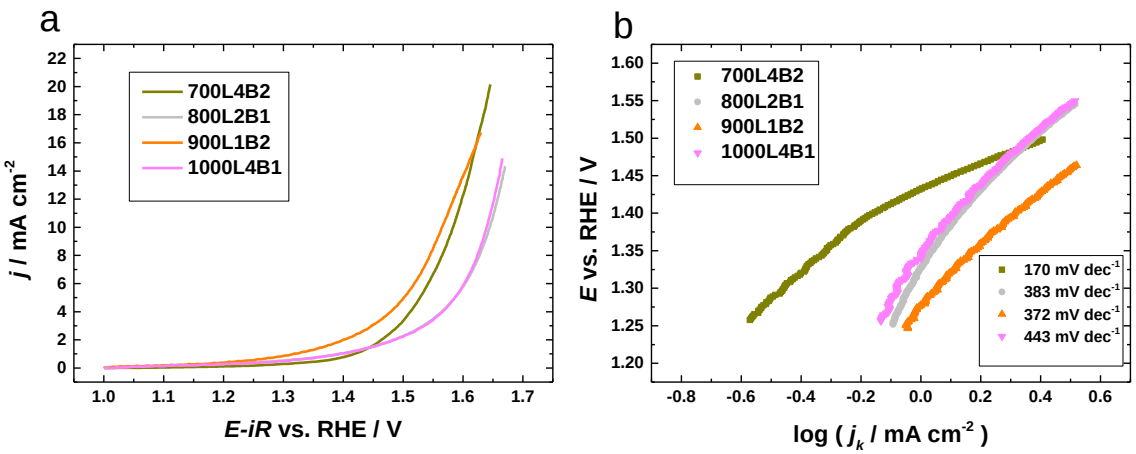

Figure 12. (a) OER polarization curves in 0.1 M KOH (under argon); v = 10 mV s^{-1}. (b) OER Tafel plots.

5.2.4. Bifunctional oxygen electroactivity

ORR and OER bifunctional electrocatalytic activities for TAL-2-based materials can be estimated by calculating the potential difference between OER and ORR ($\triangle E = E_{j=10} - E_{1/2}$, where the OER potential is taken at a current density of 10 mA cm^{-2}, while the ORR potential is taken at half-wave). It is found that sample TAL-2-700L1B2 possesses minimal $\triangle E$ of 0.736 V. The most active catalyst materials obtained in this work are compared with the results obtained for Co-N-C materials published in recent studies (Table 3). Most of these works use several precursors in order to synthesize Co-N-C electrocatalysts. The main advantage of using electron-rich TAL-2 as carbon, nitrogen and cobalt source is the possibility to use only one precursor for Co-N-C material, so it is higher possibility to obtain reproducible results.

Wang et al. have synthesized HP-CoNC-L catalyst from Zn ZIF-L, 2-Methylimidazole (2-MeIM), $Co(NO_3)_2 \cdot 6H_2O$ and using 800 °C for carbonization procedure. They concluded that rich defects and ultrafine Co nanoparticles of holey and hollow "leaf" skeleton that promoted by external foaming of cobalt ligands and the internal volatilization of zinc frame moiety had great role in high ORR/OER catalytic activity with ΔE of 0.64 V ($E_{j=10}$ = 1.53 V; $E_{1/2}$ = 0.89 V).[17] According to report of Chen et al., ZIF-L was used as a precursor to obtain Co-NCS@CNT catalyst at 700 °C carbonization temperature. The resulted catalyst showed $E_{1/2}$ of 0.86 V for ORR and overpotential of 360 mV at 10 mA cm^{-2} towards OER which was

achieved through abundant Co-N-C active sites, high electrical conductivity, large specific surface area (396 m^2 g^{-1}) and fast mass/electron transport.[18]

Table 2. Summary of electrochemical kinetic parameters of the study.

	No.	Sample Name	$E_{1/2}$ (V)	Eon (V)	$E_{j=10}$ OER (V)	ΔE (V)	n	Overpotential OER (V)	Tafel slope ORR (mV dec^{-1})	Tafel slope OER (mV dec^{-1})
B1 – 5h, 80 °C	1	TAL-2-700L1B1	0.815	0.889	1.6	0.785	4	0.36	-43	393
	2	TAL-2-700L2B1	0.784	0.886	1.7	0.916	4	0.46	-56	90
	3	TAL-2-700L3B1	0.783	0.924	1.83	1.047	4	0.59	-57	96
	4	TAL-2-700L4B1	0.764	0.897	1.83	1.066	4	0.59	-65	78
	5	TAL-2-800L1B1	0.746	0.805	1.66	0.914	4	0.42	-38	448
	6	TAL-2-800L2B1	0.85	0.944	1.65	0.8	4	0.41	-52	383
	7	TAL-2-800L3B1	0.804	0.881	1.66	0.856	4.5	0.42	-48	131
	8	TAL-2-800L4B1	0.831	0.897	1.67	0.839	3.5	0.43	-38	310
	9	TAL-2-900L1B1	0.824	0.905	1.61	0.786	4.5	0.37	-41	376
	10	TAL-2-900L2B1	0.847	0.934	1.65	0.803	4.5	0.41	-45	382
	11	TAL-2-900L3B1	0.853	0.974	1.62	0.767	4	0.38	-52	424
	12	TAL-2-900L4B1	0.818	0.917	1.77	0.952	4	0.53	-56	350
	13	TAL-2-1000L1B1	0.816	0.918	1.64	0.824	3.5	0.4	-56	374
	14	TAL-2-1000L2B1	0.818	0.917	1.65	0.832	3.9	0.41	-55	363
	15	TAL-2-1000L3B1	0.847	0.958	1.66	0.813	4	0.42	-42	400
	16	TAL-2-1000L4B1	0.83	0.906	1.64	0.81	4.1	0.4	-46	443
B2 – 8h, 50 °C	17	**TAL-2-700L1B2**	0.844	0.928	1.58	0.736	4	0.34	-46	388
	18	TAL-2-700L2B2	0.782	0.864	1.59	0.808	4	0.35	-47	306
	19	TAL-2-700L3B2	0.847	0.924	1.64	0.793	4	0.4	-47	406
	20	TAL-2-700L4B2	0.769	0.895	1.58	0.811	4.5	0.34	-68	170
	21	**TAL-2-800L1B2**	0.862	0.949	1.77	0.908	3.9-4	0.53	-53	149
	22	TAL-2-800L2B2	0.86	0.939	1.77	0.91	3.9-4	0.53	-45	115
	23	TAL-2-800L3B2	0.828	0.953	1.79	0.962	4.5	0.55	-63	157
	24	TAL-2-800L4B2	0.831	0.948	1.75	0.919	4	0.51	-62	127
	25	TAL-2-900L1B2	0.818	0.905	1.56	0.742	3.9-4	0.32	-47	372
	26	TAL-2-900L2B2	0.856	0.927	1.61	0.754	3.9-4	0.37	-43	370
	27	TAL-2-900L3B2	0.855	0.949	1.63	0.775	3.9-4	0.39	-48	363
	28	TAL-2-900L4B2	0.852	0.942	1.66	0.808	4.5	0.42	-44	309
	29	TAL-2-1000L1B2	0.847	0.928	1.67	0.823	3.85	0.43	-48	377
	30	TAL-2-1000L2B2	0.841	0.917	1.66	0.819	3.95-4	0.42	-42	446
	31	TAL-2-1000L3B2	0.813	0.917	1.65	0.837	4	0.41	-59	418
	32	TAL-2-1000L4B2	0.78	0.979	1.65	0.87	4	0.41	-65	362
B3	33	TAL-2-700B3	0.594	0.798	1.76	1.166	3.9-4	0.52	-99	76
	34	TAL-2-800B3	0.835	0.902	1.76	0.925	3.9-4	0.52	-37	118
	35	TAL-2-900B3	0.842	0.912	1.62	0.778	3.9-4	0.38	-39	349
	36	TAL-2-1000B3	0.795	0.868	1.65	0.855	3.7-4	0.41	-41	390

Moreover, Co/Co–N–C catalyst was developed from cobalt(II) chloride hexahydrate ($CoCl_2 \cdot 6H_2O$), Phen, DCDA precursors by using 500 and 800 °C carbonization temperatures by Wang and colleagues. The dual-nitrogen sources derived catalyst material exhibited $E_{1/2}$

= 0.882 V and $E_{j=10}$ = 1.64 V towards ORR and OER, respectively, due to the powerful coupling of Co–N and metallic Co species.[19]

One possible strategy involving bifunctionality proposed by Zhang et al. was design of Co/N-C_{Zn} bifunctional catalyst from PPy@$ZnCl_2$ and $[Co(NH_3)_6]Cl_3$ precursors at heat-treatment temperature of 900 °C where the $ZnCl_2$ treatment of PPy caused more micropores and defects that empower Co/N-C_{Zn} structure to have a higher amount of Co loading, extra active Co-N and pyridinic N sites, larger surface area as well. These qualities was led to ΔE of 0.76 V ($E_{j=10}$ = 1.64 V; $E_{1/2}$ = 0.88 V) which was great ORR and OER performance.[20]

Another proposed strategy by Wu et al. involves synthesis of H-Co@FeCo/N/C from ZnCo-ZIF@PDA and Fe(III) at carbonization temperature of 930 °C. The half-wave potential was 0.91 V for ORR and $E_{j=10}$ was 1.608 V for OER at 10 mA cm^{-2} due to the synergistic catalytic effect of the CoN_x and FeN_x double active sites to lessen reaction energy barrier of active metal particles.[21] Additionally, Qin et al. prepared Co_3O_{4-x}/NG catalyst by employing laser irradiation of the Co_3O_4/NG powder that demonstrated outstanding oxygen electrocatalytic performance with ΔE of 0.66 V ($E_{j=10}$ = 1.5 V; $E_{1/2}$ = 0.84 V) because of synergistic effect stemming from oxygen vacancies and Co-N-C cooperation.[22] Besides, Ding and co-workers found that CoO/Co@N−C synthesized from Co_3O_4@Glu at 900 °C pyrolysis temperature endowed higher bifunctional performance toward both ORR and OER due to several factors such as porous N-doped carbon microsphere matrix, metallic Co component and CoO.[23]

Recent work by Lv et al. suggest that $Co_2N_{0.67}$-BHPC catalyst obtained from mushroom and H_2TPP_1/CoTPP by applying heat treatment at 900 °C showed trifunctional electrocatalytic performance towards the ORR, OER and HER because of the larger surface area, fast charge transfer, increased conductivity and lots of defects of the catalyst material.[24] Zhu et al. have reported Co–N–C-0.5 (0.5 indicates the molar ratio of Zn in the initial ZIF-67) catalyst material that was synthesized from bi-ZIF-x and pyrolysed at 900 °C. It demonstrated superior activity with ΔE of 0.94 V ($E_{j=10}$ = 1.7 V; $E_{1/2}$ = 0.76 V) benefiting from rapid electron transfer, number of active sites such as CoN_x/Co composite and N-doped defective carbon.[25] Furthermore, Zhou and colleagues used CoCo-Prussian blue analogue (CoCo-PBA), graphitic carbon nitride nanosheets (GCNS), polydopamine (PDA) and sodium hypophosphite (NaH_2PO_2) to obtain CoP-NPC-800 electrocatalyst, which showed superb bifunctionality towards ORR/OER reactions because of the prompted mass/charge transfer and enhanced specific surface area (625.7 m^2 g^{-1}).[26] Duan et al. developed FeCo–N–C-700 catalyst from ZnCo–ZIF@Fe/glucosamine precursor by carbonized it at 700 °C. The resulted catalyst exhibited enhanced bifunctional performance, which could be attributed to

the synergetic effect of Co and Fe active sites.[27] Lin and co-workers synthesized CoFe@NC-700 catalyst from CoFe@ZIF and pyrolyzed it at 700 °C. The obtained catalyst showed improved electrocatalytic performance stemming from synergetic effect of Fe/Co-N, porous structure that accelerate mass transport and high surface area.[28] Moreover, Liu et al. suggested preparation of 3D-Co@Co-NPC by employing 2-methylimidazole, cobalt nitrate hexahydrate and NaH_2PO_2 precursors. The synthesized and heat-treated catalyst material showed superior performance benefiting from doping of P element to Co-N-C matrix.[29]

Table 3. Comparison of ORR/OER bifunctional activity ($\Delta E = E_{10}^{OER} – E_{1/2}^{ORR}$) for different catalysts.

Catalyst	**Precursors**	**OER E_{10} @10mA cm^{-2}**	**ORR $E_{1/2}$ @1600 rpm**	**ΔE**	**Reference**
HP-CoNC-L	Zn ZIF-L, 2-Methylimidazole (2-MeIM) $Co(NO_3)_2{\cdot}6H_2O$, 800 °C, (ORR: 0.1 M KOH; OER: 1 M KOH)	1.53	0.89	0.64	[17]
Co-NCS@CNT	ZIF-L, 700 °C, (ORR: 0.1 M KOH; OER: 1 M KOH)	1.58	0.86	~0.72	[18]
TAL-2-700L1B2	TAL2, 700 °C 0.1 M KOH	1.58	0.844	0.736	This work
TAL-2-800L1B2	TAL2, 800 °C 0.1 M KOH	1.77	0.862	0.908	This work
TAL-2-900L1B2	TAL2, 900 °C 0.1 M KOH	1.56	0.818	0.742	This work
Co/Co–N–C	Cobalt(II) chloride hexahydrate ($CoCl_2{\cdot}6H_2O$), Phen , DCDA, 500 °C, 800 °C, 0.1 M KOH	1.64	0.882	0.758	[19]
Co/N-C_{Zn}	PPy@$ZnCl_2$, $[Co(NH_3)_6]Cl_3$, 900 °C, (ORR: 0.1 M KOH; OER: 1 M KOH)	1.64	0.88	0.76	[20]
H-Co@FeCo/N/C	ZnCo-ZIF@PDA, Fe(III), 930 °C, 0.1 M KOH	1.608	0.91	0.698	[21]
Co_3O_{4-x}/NG	Co_3O_4/NG powder Laser irradiation, 1.0 M KOH	1.5	0.84	0.66	[22]
CoO/Co@N−C	Co_3O_4@Glu, 900 °C, 0.1 M KOH	1.672	0.85	~0.822	[23]
$Co_2N_{0.67}$-BHPC	Mushroom, H_2TPP_1/CoTPP, 900 °C, (ORR: 0.1 M KOH; OER: 1 M KOH)	1.57	0.86	~0.71	[24]
Co–N–C-0.5	bi-ZIF-x, 900 °C, 0.1 M KOH	1.7	0.76	0.94	[25]
CoP-NPC-800	CoCo-Prussian blue analogue, graphitic carbon nitride nanosheets, polydopamine, sodium hypophosphite, (ORR: 0.1 M KOH; OER: 1 M KOH)	1.538	0.821	0.717	[26]
FeCo–N–C-700	ZnCo-ZIF @Fe/glucosamine, 700 °C, 0.1 M KOH	1.606	0.896	0.71	[27]
CoFe@NC-700	CoFe@ZIF, 700 °C, (ORR: 0.1 M KOH; OER: 1 M KOH)	1.7	0.89	0.81	[28]
3D-Co@Co-NPC	2-methylimidazole, cobalt nitrate hexahydrate, NaH_2PO_2, 950 °C, (ORR: 0.1 M KOH; OER: 1 M KOH)	1.692	0.872	0.82	[29]

All in all, the studies that have been done to explore bifunctional electrocatalytic performance of transition-metal based materials have shown promising results toward ORR and OER reactions. To explore the nature of the superior ORR and OER activities of TAL-2 based materials, experimental data library collected for 36 samples in this work will further be utilized for theoretical modelling to explore the ORR/OER activities.

6. SUMMARY

In this work, cost-effective and highly active TAL-2-based catalyst material was obtained by organic synthesis with efficient strategy. The resulting material was optimized through different procedures such as acid leaching and carbonization to get its derivatives.

The composition and structure of derived catalysts were explored by several techniques (scanning electron microscopy, powder X-ray diffraction, X-ray photoelectron spectroscopy, Brunauer–Emmett–Teller method, and Raman spectroscopy) and electrochemical behavior of processed materials was studied in alkaline electrolyte solution towards ORR and OER to demonstrate the effect of various pyrolysis temperatures on the electrocatalytic activity of TAL-2-based catalysts.

To conclude, the particular catalyst material (TAL-2-700L1B2) that has gone through acid leaching at 50 °C for 8 h showed superior bifunctional oxygen electrocatalytic activity with smaller ΔE of 0.736 V ($E_{j=10}$ = 1.58 V; $E_{1/2}$ = 0.844 V) than rest of catalysts of this work. Additionally, TAL-2-800L1B2 demonstrated outstanding catalytic activity towards the ORR with a half-wave potential of ($E_{1/2}$) of 0.862 V and an onset potential (E_{on}) of 0.949 V, while TAL-2-900L1B2 catalyst material displayed 1.56 V for OER which was achieved at benchmark current density of 10mA cm^{-2}.

Experimental data library collected in this work will further be used for theoretical modelling.

ACKNOWLEDGEMENTS

I would like to state my gratitude to my supervisor Dr. Nadezda Kongi for her supervision, and given support throughout the project.

I would like to thank Dr. Maike Käärik (UT) and Dr. Jaan Leis (UT) for the BET measurement, Dr. Jaan Aruväli (UT) for the PXRD measurements, Dr. Pavel Starkov and Dr. Kefeng Ping (TalTech) for TAL-2 precursors and Raman, Dr. Tanel Käämbre (UT) for XPS measurements and Dr. Kaido Tammeveski for his support and research conduction opportunity.

This work was supported by the Estonian Research Council grant (PSG250).

REFERENCES

(1) Song, C.; Zhang, J. Electrocatalytic Oxygen Reduction Reaction. In *PEM Fuel Cell Electrocatalysts and Catalyst Layers*; Zhang, J., Ed.; Springer London: London, 2008; pp 89–134. https://doi.org/10.1007/978-1-84800-936-3_2.

(2) Ge, X.; Sumboja, A.; Wuu, D.; An, T.; Li, B.; Goh, F. W. T.; Hor, T. S. A.; Zong, Y.; Liu, Z. Oxygen Reduction in Alkaline Media: From Mechanisms to Recent Advances of Catalysts. *ACS Catal.* **2015**, *5* (8), 4643–4667. https://doi.org/10.1021/acscatal.5b00524.

(3) Du, C.; Sun, Y.; Shen, T.; Yin, G.; Zhang, J. Applications of RDE and RRDE Methods in Oxygen Reduction Reaction. In *Rotating Electrode Methods and Oxygen Reduction Electrocatalysts*; Elsevier, 2014; pp 231–277. https://doi.org/10.1016/B978-0-444-63278-4.00007-0.

(4) Si, F.; Zhang, Y.; Yan, L.; Zhu, J.; Xiao, M.; Liu, C.; Xing, W.; Zhang, J. Electrochemical Oxygen Reduction Reaction. In *Rotating Electrode Methods and Oxygen Reduction Electrocatalysts*; Elsevier, 2014; pp 133–170. https://doi.org/10.1016/B978-0-444-63278-4.00004-5.

(5) Senarathna, K. G. C.; Randiligama, H. M. S. P.; Rajapakse, R. M. G. Preparation, Characterization and Oxygen Reduction Catalytic Activities of Nanocomposites of Co(II)/Montmorillonite Containing Polypyrrole, Polyaniline or Poly(Ethylenedioxythiophene). *RSC Adv.* **2016**, *6* (114), 112853–112863. https://doi.org/10.1039/C6RA23100D.

(6) Khotseng, L. Oxygen Reduction Reaction. In *Electrocatalysts for Fuel Cells and Hydrogen Evolution - Theory to Design*; Ray, A., Mukhopadhyay, I., K. Pati, R., Eds.; IntechOpen, 2018. https://doi.org/10.5772/intechopen.79098.

(7) Ghosh, S. K.; Rahaman, H. Noble Metal–Manganese Oxide Hybrid Nanocatalysts. In *Noble Metal-Metal Oxide Hybrid Nanoparticles*; Elsevier, 2019; pp 313–340. https://doi.org/10.1016/B978-0-12-814134-2.00009-7.

(8) Suen, N.-T.; Hung, S.-F.; Quan, Q.; Zhang, N.; Xu, Y.-J.; Chen, H. M. Electrocatalysis for the Oxygen Evolution Reaction: Recent Development and Future Perspectives. *Chem. Soc. Rev.* **2017**, *46* (2), 337–365. https://doi.org/10.1039/C6CS00328A.

(9) Tahir, M.; Pan, L.; Idrees, F.; Zhang, X.; Wang, L.; Zou, J.-J.; Wang, Z. L. Electrocatalytic Oxygen Evolution Reaction for Energy Conversion and Storage: A Comprehensive Review. *Nano Energy* **2017**, *37*, 136–157. https://doi.org/10.1016/j.nanoen.2017.05.022.

(10) Shi, Q.; Zhu, C.; Du, D.; Lin, Y. Robust Noble Metal-Based Electrocatalysts for Oxygen Evolution Reaction. *Chem. Soc. Rev.* **2019**, *48* (12), 3181–3192. https://doi.org/10.1039/C8CS00671G.

(11) Huang, Z.-F.; Wang, J.; Peng, Y.; Jung, C.-Y.; Fisher, A.; Wang, X. Design of Efficient Bifunctional Oxygen Reduction/Evolution Electrocatalyst: Recent Advances and Perspectives. *Adv. Energy Mater.* **2017**, *7* (23), 1700544. https://doi.org/10.1002/aenm.201700544.

(12) Chen, B.; Ma, G.; Zhu, Y.; Xia, Y. Metal-Organic-Frameworks Derived Cobalt Embedded in Various Carbon Structures as Bifunctional Electrocatalysts for Oxygen Reduction and Evolution Reactions. *Sci Rep* **2017**, *7* (1), 5266. https://doi.org/10.1038/s41598-017-05636-y.

(13) Du, L.; Xing, L.; Zhang, G.; Sun, S. Metal-Organic Framework Derived Carbon Materials for Electrocatalytic Oxygen Reactions: Recent Progress and Future Perspectives. *Carbon* **2020**, *156*, 77–92. https://doi.org/10.1016/j.carbon.2019.09.029.

(14) Hussain, S.; Kongi, N.; Treshchalov, A.; Kahro, T.; Rähn, M.; Merisalu, M.; Tamm, A.; Sammelselg, V.; Tammeveski, K. Enhanced Oxygen Reduction Reaction Activity and Durability of Pt Nanoparticles Deposited on Graphene-Coated Alumina Nanofibres. *Nanoscale Adv.* **2021**, *3* (8), 2261–2268. https://doi.org/10.1039/D1NA00007A.
(15) Cheng, W.; Yuan, P.; Lv, Z.; Guo, Y.; Qiao, Y.; Xue, X.; Liu, X.; Bai, W.; Wang, K.; Xu, Q.; Zhang, J. Boosting Defective Carbon by Anchoring Well-Defined Atomically Dispersed Metal-N4 Sites for ORR, OER, and Zn-Air Batteries. *Applied Catalysis B: Environmental* **2020**, *260*, 118198. https://doi.org/10.1016/j.apcatb.2019.118198.
(16) Pokhrel, S.; Shresta, M.; Slouf, M.; Sirc, J.; Adhikari, R. Eco-Friendly Urea-Formaldehyde Composites Based on Corn Husk Cellulose Fiber. *International Journal of Composite Materials* **2020**, *10(2)*, 29–36. https://doi.org/10.5923/j.cmaterials.20201002.01.
(17) Wang, J.; Liu, D.; Zhang, L.; Qian, Y.; Chen, C.; Wang, L.; Lei, W. Rational Design of 2D Super Holey Metal Carboniride Leaf-like Nanostructure for Efficient Oxygen Electrocatalysis. *Carbon* **2020**, *164*, 287–295. https://doi.org/10.1016/j.carbon.2020.04.014.
(18) Chen, D.; Yu, J.; Cui, Z.; Zhang, Q.; Chen, X.; Sui, J.; Dong, H.; Yu, L.; Dong, L. Hierarchical Architecture Derived from Two-Dimensional Zeolitic Imidazolate Frameworks as an Efficient Metal-Based Bifunctional Oxygen Electrocatalyst for Rechargeable Zn–Air Batteries. *Electrochimica Acta* **2020**, *331*, 135394. https://doi.org/10.1016/j.electacta.2019.135394.
(19) Wang, D.; Yang, P.; Xu, H.; Ma, J.; Du, L.; Zhang, G.; Li, R.; Jiang, Z.; Li, Y.; Zhang, J.; An, M. The Dual-Nitrogen-Source Strategy to Modulate a Bifunctional Hybrid Co/Co–N–C Catalyst in the Reversible Air Cathode for Zn-Air Batteries. *Journal of Power Sources* **2021**, *485*, 229339. https://doi.org/10.1016/j.jpowsour.2020.229339.
(20) Zhang, D.; Sun, P.; Zhou, Q.; Li, B.; Wei, Y.; Gong, T.; Huang, N.; Lv, X.; Fang, L.; Sun, X. Enhanced Oxygen Reduction and Evolution in N-Doped Carbon Anchored with Co Nanoparticles for Rechargeable Zn-Air Batteries. *Applied Surface Science* **2021**, *542*, 148700. https://doi.org/10.1016/j.apsusc.2020.148700.
(21) Wu, Y.; Wu, X.; Tu, T.; Zhang, P.; Li, J.; Zhou, Y.; Huang, L.; Sun, S. Controlled Synthesis of FeNx-CoNx Dual Active Sites Interfaced with Metallic Co Nanoparticles as Bifunctional Oxygen Electrocatalysts for Rechargeable Zn-Air Batteries. *Applied Catalysis B: Environmental* **2020**, *278*, 119259. https://doi.org/10.1016/j.apcatb.2020.119259.
(22) Qin, J.; Liu, Z.; Wu, D.; Yang, J. Optimizing the Electronic Structure of Cobalt via Synergized Oxygen Vacancy and Co-N-C to Boost Reversible Oxygen Electrocatalysis for Rechargeable Zn-Air Batteries. *Applied Catalysis B: Environmental* **2020**, *278*, 119300. https://doi.org/10.1016/j.apcatb.2020.119300.
(23) Ding, Y.; Yang, W.; Gao, S.; Sun, W.; Sun, C.; Li, Q. Strongly Cooperative Nano-CoO/Co Active Phase in Hierarchically Porous Nitrogen-Doped Carbon Microspheres for Efficient Bifunctional Oxygen Electrocatalysis. *ACS Appl. Energy Mater.* **2020**, *3* (2), 1328–1337. https://doi.org/10.1021/acsaem.9b01660.
(24) Lv, X.; Xiao, Z.; Wang, H.; Wang, X.; Shan, L.; Wang, F.; Wei, C.; Tang, X.; Chen, Y. In Situ Construction of Co/N/C-Based Heterojunction on Biomass-Derived Hierarchical Porous Carbon with Stable Active Sites Using a Co-N Protective Strategy for High-Efficiency ORR, OER and HER Trifunctional Electrocatalysts. *Journal of Energy Chemistry* **2021**, *54*, 626–638. https://doi.org/10.1016/j.jechem.2020.06.040.
(25) Zhu, J.; Qu, T.; Su, F.; Wu, Y.; Kang, Y.; Chen, K.; Yao, Y.; Ma, W.; Yang, B.; Dai, Y.; Liang, F.; Xue, D. Highly Dispersed Co Nanoparticles Decorated on a N-Doped

Defective Carbon Nano-Framework for a Hybrid Na–Air Battery. *Dalton Trans.* **2020**, *49* (6), 1811–1821. https://doi.org/10.1039/C9DT04073K.
(26) Zhou, X.; Xu, L.; Gao, Y.; Li, L.; Tang, J.; Yang, J. Phosphorization of a Prussian Blue Analogue-Derived Co–N–C Catalyst for Synchronously Boosting the Oxygen Reduction and Evolution Reactions. *Sustainable Energy Fuels* **2020**, *4* (5), 2411–2421. https://doi.org/10.1039/D0SE00156B.
(27) Duan, X.; Ren, S.; Pan, N.; Zhang, M.; Zheng, H. MOF-Derived Fe,Co@N–C Bifunctional Oxygen Electrocatalysts for Zn–Air Batteries. *J. Mater. Chem. A* **2020**, *8* (18), 9355–9363. https://doi.org/10.1039/D0TA02825H.
(28) Lin, Q.; Shang, C.; Chen, Z.; Akinoglu, E. M.; Wang, X.; Zhou, G. Fe-Doped Co-N/C as Effective Electrocatalyst for Oxygen Reaction. *Mater. Res. Express* **2020**, *7* (8), 085002. https://doi.org/10.1088/2053-1591/abaa8d.
(29) Liu, B.; Li, J.-Z.; Gong, X.-F.; Zhang, Y.-L.; Zhou, Q.-Y.; Cai, J.-J.; Liu, Z.-G.; Sui, X.-L.; Wang, Z.-B. Facile Synthesis of Flower-like Dual-Metal (Co/Zn) MOF-Derived 3D Porous Co@Co-NPC as Reversible Oxygen Electrocatalyst for Rechargeable Zinc-Air Batteries. *Ionics* **2020**, *26* (4), 1913–1922. https://doi.org/10.1007/s11581-019-03364-z.

Non-Exclusive Licence to Reproduce Thesis and Make Thesis Public

I, Gulnara Yusibova

1. herewith grant the University of Tartu a free permit (non-exclusive licence) to reproduce, for the purpose of preservation, including for adding to the DSpace digital archives until the expiry of the term of copyright,

"Surface Morphology Effects on Bifunctional Oxygen Electroactivity of TAL2-based Materials" supervised by Assoc. Prof. Nadezda Kongi and Assoc. Prof. Kaido Tammeveski.

2. I grant the University of Tartu a permit to make the work specified in p. 1 available to the public from ***11/06/2024*** via the web environment of the University of Tartu, including via the DSpace digital archives, under the Creative Commons licence CC BY NC ND 3.0, which allows, by giving appropriate credit to the author, to reproduce, distribute the work and communicate it to the public, and prohibits the creation of derivative works and any commercial use of the work until the expiry of the term of copyright.

3. I am aware of the fact that the author retains the rights specified in p. 1 and 2.

4. I certify that granting the non-exclusive licence does not infringe other persons' intellectual property rights or rights arising from the personal data protection legislation.

Gulnara Yusibova

04/06/2021